Exosome-Mimetic Supramolecular Vesicles with Reversible and Controllable Fusion and Fission

Jie Li, Kang Peng, Youmei Li, Jianxing Wang, Jianbin Huang, Yun Yan,[*] Dong Wang,[*] Ben Zhong Tang[*]

Dr. J. Li, Dr. Y. Li, Dr. J. Wang, Prof. D. Wang

Center for AIE Research

College of Materials Science and Engineering

Shenzhen University, Shenzhen 518060, China

E-mail: wangd@szu.edu.cn

Dr. J. Li, Dr. Y. Li, Dr. J. Wang

College of Physics and Optoelectronic Engineering

Shenzhen University, Shenzhen 518060, China

Dr. J. Li, K. Peng, Prof. J. Huang, Prof. Y. Yan

Beijing National Laboratory for Molecular Sciences (BNLMS)

College of Chemistry and Molecular Engineering

Peking University, Beijing 100871, China

E-mail: yunyan@pku.edu.cn

Prof. B. Z. Tang

Hong Kong Branch of Chinese National Engineering Research Center for Tissue Restoration and Reconstruction

Department of Chemistry

The Hong Kong University of Science and Technology, Clear Water Bay, Kowloon, Hong Kong, China

E-mail: tangbenz@ust.hk

Abstract

The fusion and fission behaviors of exosomes are essential for the cell-to-cell communication. Developing exosome-mimetic vesicles with such behaviors is of vital importance, but still remains a big challenge. Herein, we present an artificial supramolecular vesicle that exhibits redox-modulated reversible fusion-fission functions. These vesicles tend to fuse together and form large-sized vesicles upon oxidation, while undergo a fission process and return to small-sized vesicles through

reduction. Noteworthy, the aggregation-induced emission (AIE) characteristics of the supramolecular building blocks enable the molecular configuration during vesicular transformation to be monitored by fluorescence technology. Moreover, the presented vesicles are excellent nanocarrier candidates to transfer siRNA into cancer cells.

Keywords : Supramolecular vesicles, Aggregation-induced emission, Exosome-mimetic, Reversible, Fission and fusion

Introduction

Exosomes refer to the nano-sized extracellular vesicles that are closely related to intercellular signaling and substances transport.[1]. A fission process of releasing new vesicles from one cell and a fusion process of uptake by another cell are normally involved during cell-to-cell communication, and such two processes are generally reversible and controllable in living organelles.[2] However, the knowledge on membrane behaviors of fusion and fission processes, as well as their modulating factors still remains sparse due to the complex composition of exosomes and cellular environment.[3] This obstacle inspires the development of artificial vesicles that possess similar architecture and behaviors as exosomes, which not only contribute to fundamental understanding of these processes of exosomes, but also provide opportunities for practical applications of artificial vesicles as delivery in biosystems.

Despite great progresses have been made on design and creation of artificial vesicles with fusion or fission behaviors, these are always one-way transformations.[4] For instance, Paxton' group demonstrated the fusion process of a nano-sized polymersome into giant vesicles in dilute NaCl solutions.[5] Han' group developed a cell-sized vesicle loaded with DNA to mimic the division behavior of eukaryotic cells.[6] To the best of our knowledge, there

have been no previous reports on utilization of artificial vesicles to mimic the reversible and controllable fusion and fission behaviors of exosomes. In most cases, the fusion or fission processes are extensively driven by chemical reaction or osmotic stress with a simple method of adding substrates (such as salt, glucose, proteins, *et al.*) into aqueous solutions.[4i,5] The chemical reaction and osmotic stress offer sufficient energy to change surface tension of membrane and water volume inside vesicles, generating the subsequent morphological transformations. However, the reversible transformation is difficult to be realized, mainly because these chemical reactions are irreversible and few approaches can be explored to decrease osmotic stress outside vesicles to original state. Evidently, the exploration of artificial vesicles with reversible and controllable fusion and fission behaviors as exosomes is a definitely appealing yet significantly challenging task.

Herein, a novel Fe^{2+}-coordinated supramolecular vesicle was facilely fabricated by using aggregation-induced emission (AIE)-active molecules as building blocks. As illustrated in Scheme 1, the vesicle underwent a fusion process upon oxidation of Fe^{2+} to Fe^{3+}, while a fission process further proceeded when Fe^{3+} was reduced to Fe^{2+}, demonstrating the reversible fusion and fission behaviors modulated by redox reaction. Noteworthy, the AIE characteristics allow us to monitor the molecular configuration during vesicular transformation via fluorescence technology.[7] Moreover, these vesicles can serve as nanocarrier to transfer siRNA into cancer cells. This study presents an important step forward toward the development of artificial cellular membrane.

TPE-BPA

CTAB

Fe^{2+}

Self-assembly

Oxidation (fusion)
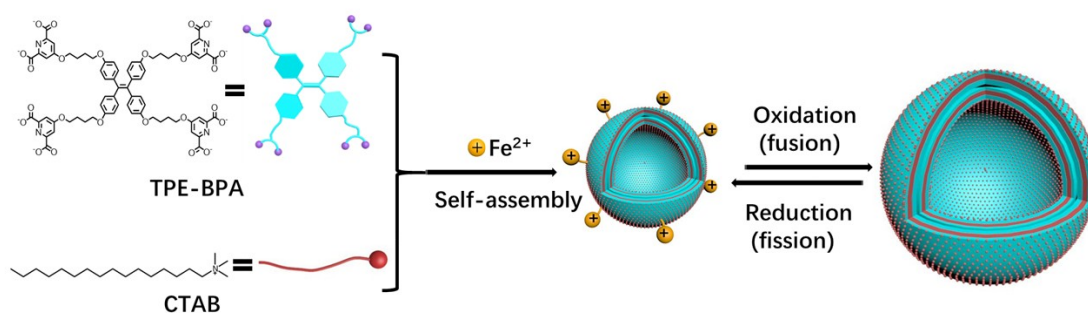
Reduction (fission)

Scheme 1. Schematic illustration of construction of exosome-mimetic vesicles, and their reversible and controllable fusion-fission behaviors.

The Fe^{2+}-coordinated vesicles were constructed through self-assembly of AIE-active TPE-BPA, cetyltrimethylammonium bromide (CTAB) and Fe^{2+} ions (Scheme 1). TPE-BPA is a negative charged tetra-armed molecule, which exhibits strong fluorescent emission in aggregated states. It is able to spontaneously self-assemble into neutral fluorescent vesicles through integrating with eight positively charged CTAB molecules via ionic interaction.[8] The coordinating heads of TPE-BPA make the TPE-BPA@8CTAB supramolecular vesicles capable to coordinate with many metal ions, such as Fe^{2+} and Fe^{3+}.[9] It was observed that with continuously adding Fe^{2+} ions into TPE-BPA@8CTAB vesicles solution, the Zeta potentials and UV absorption of coordinating heads (255 nm) remarkably increased and reached a platform at the molar ratio of TPE-BPA: Fe^{2+} = 1: 2 (Figure S1), implying the coordination between vesicle and Fe^{2+} ions. Transmission electron microscopy (TEM) observation and dynamic laser scattering (DLS) in Figure 1A and S2 revealed that Fe^{2+}@vesicle had well-defined vesicular structures with an average radius of 25 nm. Atomic force microscopic (AFM) image showed that Fe^{2+}@vesicles were spherical particles, and the present concave feature confirmed the vesicular structures of Fe^{2+}@vesicle (Figure S3). Considering the collapsed structure in AFM images, the thickness of the vesicular membrane was half of the measured height from their AFM images (Figure S3), which were calculated to be ∼10.1 nm and 7.5 nm. Since the molecular lengths of TPE-BPA and CTAB were respectively calculated to be around 2.5 nm and 2.0 nm, the vesicle-like structures might possess a multilayer structure, where TPE-BPA acted as the framework of membrane. Similarly, after addition of same amount of Fe^{3+} into TPE-BPA@8CTAB vesicles solution, Fe^{3+}@vesicle showed vesicular structures as well (Figure S2), and AFM images also demonstrated the collapsed vesicular structure (Figure S4). In addition, the average radius and Zeta potential of Fe^{3+}@vesicles were determined to be 54 nm (Figure 1A) and 3 mV (Figure 1D), respectively.
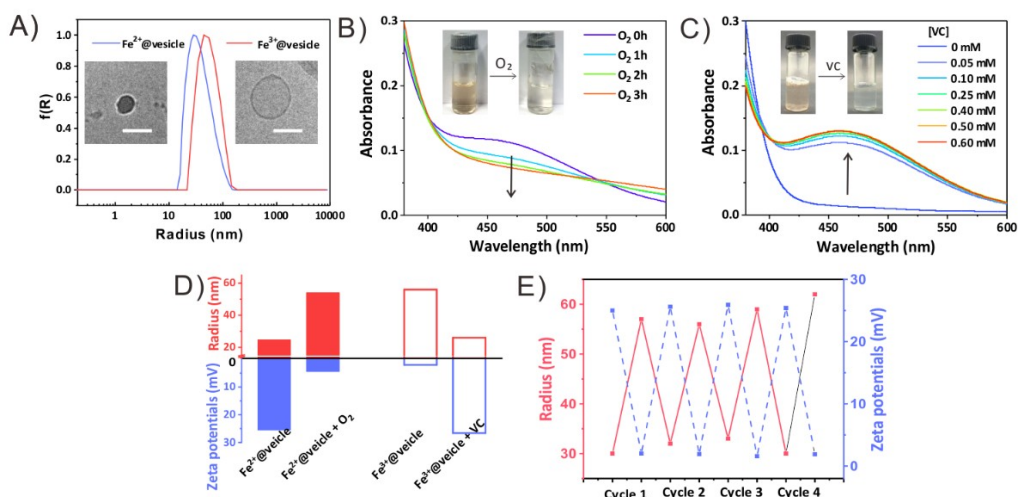
Figure 1. (A) DLS results of Fe^{2+}@vesicles and Fe^{3+}@vesicles. Inserted pictures are Cryo-TEM images of Fe^{2+}@vesicles and Fe^{3+}@vesicles. Scale bar is 100 nm. UV spectra of (B) Fe^{2+}@vesicles upon exposure to O_2 and (C) Fe^{3+}@vesicles with addition of VC. (D) Radius and Zeta potentials variation of Fe^{2+}@vesicles upon exposure to O_2 and Fe^{3+}@vesicles with addition of VC. (E) Reversible size and charged state change of the Fe^{2+}@vesicles upon the alternate addition of VC and O_2.

Despite Fe^{2+}@vesicle and Fe^{3+}@vesicle showed identical vesicular structures, their differences in size distribution and Zeta potentials inspired us to modulate their reversible transformation via redox treatment. By bubbling O_2 to the Fe^{2+}@vesicle, the UV absorption at 462 nm that was the specific coordination characteristic between Fe^{2+} and coordinating group of TPE-BPA gradually decreased (Figure 1B), suggesting the disappearance of this coordination[10], which was also confirmed by the colour change of solution from dark yellow to colourless. X-ray photoelectron spectroscopy (XPS) measurement further showed that the Fe^{2+} has been oxidized into Fe^{3+} (Figure S5). Additionally, upon bubbling O_2 to the Fe^{2+}@vesicle, the Zeta potentials of vesicles decreased from 25 mV to 5 mV (Figure 1D), accompanied with a vesicular radius increase from 25 nm to 54 nm (Figure 1E). Meanwhile, TEM observation revealed that the vesicles obtained from oxidation had exactly the same structure as those directly prepared from Fe^{3+} (Figure S6A). These results definitely demonstrated that Fe^{2+}@vesicle was transformed into Fe^{3+}@vesicle. It was observed that with addition of reductive Vitamin C (VC) to Fe^{3+}@vesicle system, UV absorption at 462

nm increased gradually, indicating the appearance of coordination between Fe^{2+} and TPE-BPA (Figure 1C). Simultaneously, all the Zeta potentials, size of vesicles and the morphology observed in TEM images of these generated vesicles were the same as the Fe^{2+}@vesicles (Figure 1D and S6B), which strongly suggested that Fe^{3+}@vesicle was reduced to Fe^{2+}@vesicle by VC. Furthermore, the redox cycle between Fe^{2+}@vesicle and Fe^{3+}@vesicle can be reproduced for many times, which was witnessed by the alternative changes of both Zeta potential and size of the vesicle (Figure 1E). As depicted by the TEM and AFM images (Figure S7), the vesicle morphology always remained constant during the repeated cycles. Combining all the results above, it seemed reasonable to infer that the transformation between Fe^{2+}@vesicle and Fe^{3+}@vesicle could be reversibly and controllably achieved by redox reaction.

Given that the original TPE-BPA@CTAB vesicle was nearly charge neutral, it was understandable that binding of Fe^{2+} would increase the zeta potential of the vesicle. However, it was rather surprising that binding of Fe^{3+}, which carried higher charges than the Fe^{2+}, didn't change the zeta potential of the vesicle very much. This can be attributed to the hydrolysis of Fe^{3+} ions under the experimental condition (pH = 6). Indeed, theoretical analysis indicated that under the experimental pH condition, around 78% Fe^{3+} existed in the form of non-charged $Fe(OH)_3$ while the 21% was in the form of $Fe(OH)_2^+$ and 1% was $Fe(OH)^{2+}$ (Figure S8). However, at the same pH condition, Fe^{2+} was not hydrolysed at all. Since the hydrolysed species $Fe(OH)_n^{(3-n)+}$ had weaker binding ability to the TPE-BPA vesicle, only few Fe^{3+} species were coordinated to increase the surface charges of Fe^{3+}@vesicle. This was proved by identical size and Zeta potential results between Fe^{3+}@vesicle and original vesicles (Figure S9), as well as the unchanged UV absorption (Figure S10). In addition, compared to Fe^{2+}@vesicle, Fe^{3+}@vesicle had a much indistinct contrast difference in membrane in TEM images, which suggested that few Fe^{3+} ions were bound to Fe^{3+}@vesicles while a large amount of Fe^{2+} ions were located in Fe^{2+}@vesicle.

The redox reaction and hydrolysis could slow down the transformation,

which provide opportunities to investigate the reversible processes. Real-time DLS measurement demonstrated that the scattered light intensity gradually decreased when sustaining bubbling O_2 into Fe^{2+}@vesicle solutions, which accompanied with gradual enlargement of the radius of vesicles over time (Figure 2A and 2B). For example, with bubbling O_2 for 1.5 h, the scattered light intensity decreased from 162 to 140 kcps, and the radius of vesicles raised from 25 to 35 nm. The scattered light intensity is proportional to the number density and particle size of vesicles, therefore, the decrease of scattered intensity and increase of particle size would cause a significant reduce of number density of particles. This suggested that small vesicles may fuse into large vesicles during the oxidizing process. The fusion process was confirmed by TEM images where some small vesicles were fusing to form large bead-like structure (Figure 2C). Similarly, when VC was added into Fe^{3+}@vesicle solution, the scattered light intensity gradually increased over time and reached a platform within 25 min, simultaneously a decrease of vesicles size occurred (Figure 2D and 2E). The abnormal increase of scattered intensity in the smaller Fe^{2+}@vesicle system could be mainly ascribe to the increased particle population, suggesting that fission behaviour might occur in the reduction process. Interestingly, TEM images clearly demonstrated the fission, in which a small vesicle was budding from the large vesicle (Figure 2F).
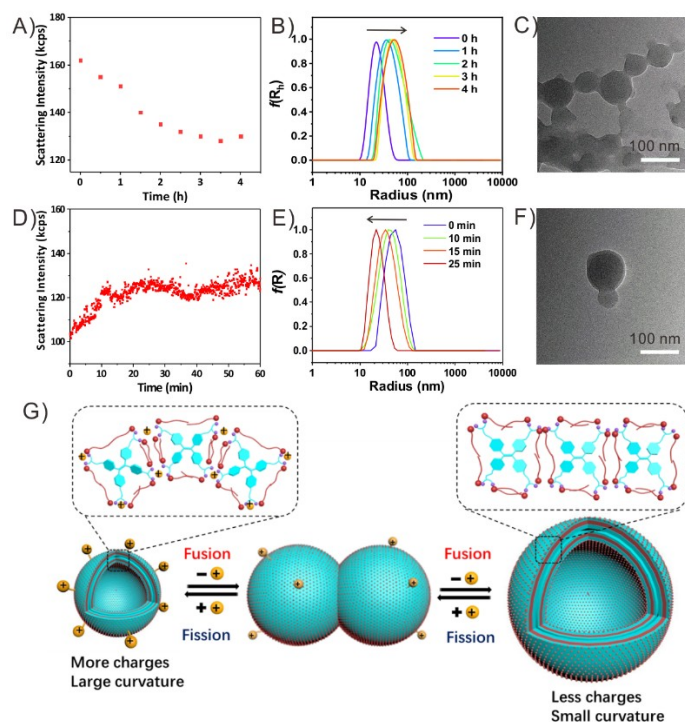
Figure 2. (A) Real-time scattering intensity change and (B) size distribution of Fe^{2+}@vesicles exposed to O_2. (C) TEM images of fusion behaviors of Fe^{2+}@vesicles upon oxidation. (D) Real-time scattering intensity change and (E) size distribution of fission behaviors of Fe^{3+}@vesicles with VC. (F) TEM images of fission process of Fe^{2+}@vesicles upon reduction. (G) Schematic illustration of mechanism reversible and controllable fusion and fission behaviors.

The possible mechanism of reversible and controllable fusion and fission behaviours was illustrated in Figure 2G. In Fe^{2+}@vesicle, due to the strong electrostatic repulsive interaction of positively charges produced by coordination of Fe^{2+} ions, TPE-BPA molecules tended to repel each other and stacked in loose states. As a result, the vesicles possessed a large curvature in membrane and a small radius. When the Fe^{2+} was oxidized to Fe^{3+} by O_2, positive charges and electrostatic repulsive force drastically weakened, resulting in the compact stacking of vesicle membrane, as most of the Fe^{3+} ions were hydrolysed and the yielded hydrates showed negligible coordinated capacity. Consequently, vesicles fused together to lower their interaction free energy and formed large-sized vesicles with small curvature. Inversely, upon the reduction by adding VC, Fe^{3+} and their hydrates were transformed to Fe^{2+} ions, which hold an excellent coordinated capacity to vesicles. The increased electrostatic

repulsive force could cause the fission of vesicles, and subsequently generated small-sized vesicles with large curvature. Thus, the vesicles reverted back to their original state in the fission process via reduction. To check the dominant role of charges on fission and fusion of vesicles, Edetate disodium (EDTA) that has stronger coordination capability with Fe^{2+} than TPE-BPA was employed to remove metal ions. With stepwise addition of EDTA into Fe^{2+}@vesicle solution, the fluorescence of the vesicles was gradually increased (Figure 3A), which suggested that Fe^{2+} ions were removed from vesicle because Fe^{2+} was able to quench the fluorescent emission. Moreover, the increase of radius and decrease of Zeta potentials of vesicles upon the addition of EDTA also demonstrated the vesicle fusion caused by the removal of charges (Figure S11). When 0.25 mM EDTA was added, the vesicles showed the same Zeta potential, radius and morphology as TPE-BPA@CTAB vesicles (Figure 3B), indicating that Fe^{2+}@vesicle recovered to the original vesicles by removal of charges.

Supramolecular materials based on AIE molecules display strong fluorescent emission, and the change of fluorescence is usually related to the rearrangement of AIE molecules.[11] This provides us a convenient and sensitive protocol to monitor the molecular packing architecture during vesicular transformation. Because of the inherent obstacles of fluorescence quenching caused by both Fe^{2+} and Fe^{3+} ions, Co^{2+} ions were utilized for the evaluation. TPE-BPA@8CTAB vesicle was a charge-neutral vesicle with strong fluorescent emission. The stepwise addition of Co^{2+} ions induced the decrease in size of vesicles and the increase in Zeta potentials, corresponding to fission process caused by charges (Figure 3D). Meanwhile, the gradually decreased fluorescent emission accompanying with a blue shift from 486 nm to 455 nm was observed (Figure 3C). These results indicated that AIE molecules possessed a more twisted configuration and stacked loosely to each other in Co^{2+}@vesicles. On the contrary, when EDTA was added to Co^{2+}@vesicles solution aiming to remove the charges in membrane, both increased size and decreased Zeta potentials were determined, implying the occurrence of vesicle fusion (Figure 4F), where the fluorescent emission gradually increased with a red emission shift from 455 nm to

488 nm (Figure 4E). Combined with TEM images (Figure S12), these results further confirmed the supposed mechanism towards fusion and fission behaviours of the vesicles.
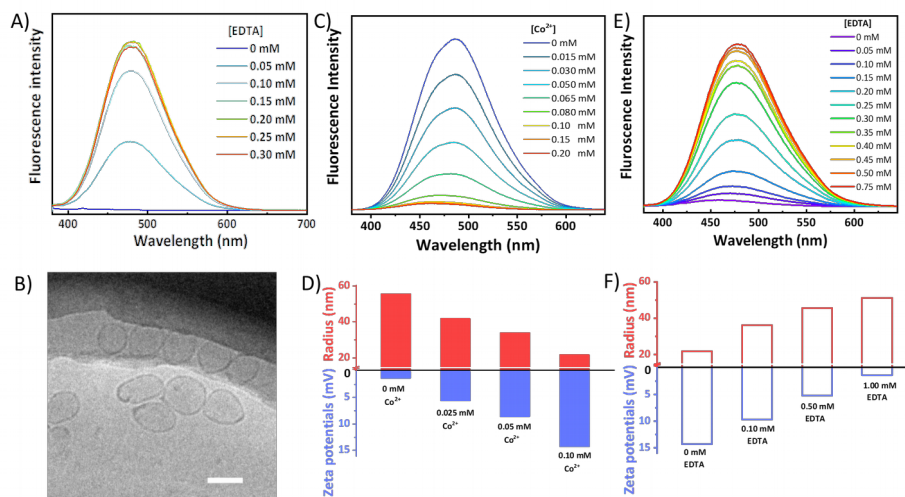
Figure 3. (A) Fluorescence of Fe^{2+}@vesicles with addition of EDTA. (B) Cryo-TEM images of Fe^{2+}@vesicles with 0.25 mM EDTA. Scale bar is 100 nm. (C) Fluorescence intensity and (D) Zeta potentials-radius changes of vesicles with addition of Co^{2+}. (E) Fluorescence intensity and (F) Zeta potentials-radius variation of Co^{2+}@vesicles with addition of EDTA.

Substances with critical role in living systems could be encapsulated in exosomes and transferred into cells, which stimulated us to take the exosome-mimetic vesicles for drug delivery. As one of the most promising agents for cancer therapy, siRNA plays important role in repairing the destroyed biosystems. However, efficient delivery is generally required because of the low cellular uptake of siRNA.[12] Benefiting from the negatively charged feature of siRNA, positive Fe^{2+}@vesicle is potentially powerful as nanocarrier for siRNA. Upon the addition of siRNA into Fe^{2+}@vesicle solution, the Zeta potential decreased from 25 mV to -5 mV, solidly suggesting the binding of siRNA to vesicles (Figure S13). To straightforwardly track the cellular uptake of siRNA, red-emissive dye Cy5 was used to label siRNA. As depicted in Figure 4 and S14, negligible fluorescent signal was observed in cells when bare siRNA without vesicles was incubated in the cell culture. On the contrary, the cells exhibited bight emission after incubating siRNA-loaded Fe^{2+}@vesicle for the same period. These outcomes obviously revealed that the utilization of Fe^{2+}@vesicle

indeed promoted the delivering siRNA to cells. On account of the oxidative intracellular environment of cancer cells,[13] the cell-engulfed Fe^{2+}@vesicle can be oxidized to Fe^{3+}@vesicle and consequentially lead to the release of siRNA in cancer cells. The Agarose gel electrophoresis results showed that siRNA was indeed released under oxidative condition, and a longer bubbling time of O_2 induced a larger amount of siRNA to be released (Figure S15A). Furthermore, the therapeutic efficiency of siRNA loaded Fe^{2+}@vesicle was investigated by quantitatively evaluating on HeLa cancer cells. The study of dose-dependent cytotoxicity revealed that cancer cell viability was gradually and rapidly decreased with raising the concentration of siRNA loaded Fe^{2+}@vesicles, as illustrated in Figure S15B, 2 μM of siRNA loaded Fe^{2+}@vesicles could cause almost complete cell death with only 7% of cell viability remained. These results demonstrated that Fe^{2+}@vesicles were considerably powerful template for drug delivery.
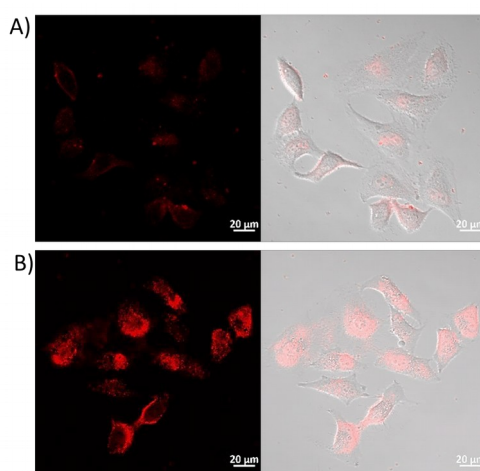
Figure 4. Fluorescence imaging of (A) bare siRNA and (B) siRNA loaded Fe^{2+}@vesicles after incubated in Hela cells for 4 h.

We have successfully fabricated an exosome-mimetic vesicle with reversible fusion and fission behaviours that could be controlled by redox. The charges of vesicle played a significant role in vesicular transformation. When Fe^{2+} was oxidized to Fe^{3+} by O_2, positive charges were removed from vesicle because of the hydrolysis-induced decrease of coordinated capacity. Consequently, vesicles trended to fuse together and form large-sized vesicles to lower the intension free energy. Inversely,

upon reduction of Fe^{3+} to Fe^{2+}, the enhanced electrostatic repulsive force lead to the formation of small-sized vesicles through fission process. Moreover, benefiting from the AIE features of the vesicle building blocks, the molecular packing states in vesicular transformation can be straightforwardly monitored by fluorescence emission changes. The presented vesicles could also perform as nanocarrier for siRNA. This study would thus provide innovative understanding for the fusion and fission behaviors of exosomes, and give us a blueprint for the next generation of drug delivery system.

Conflict of interest

The authors declare no conflict of interest.

Reference

[1] a) L. Alvarez-Erviti, Y. Seow, H. Yin, C. Betts, S. Lakhal, M. J. A. Wood, *Nat. Biotechnol.* **2011**, *29*, 341-345; b) X. Zhou, F. Xie, L. Wang, L. Zhang, S. Zhang, M. Fang, F. Zhou, *Cell. Mol. Immunol.* **2020**, *17*, 323-334; c) C. Théry, L. Zitvogel, S. Amigorena, *Nat. Rev. Immunol.* **2002**, *2*, 569-579; d) H. Valadi, K. Ekström, A. Bossios, M. Sjöstrand, J. J. Lee, J. O. Lötvall, *Nat. Cell Biol.* **2007**, *9*, 654-659; e) Z. G. Zhang, B. Buller, M. Chopp, *Nat. Rev. Neurol.* **2019**, *15*, 193-203; f) C. V. Harding, J. E. Heuser, P. D. Stahl, *J. Cell. Biol.* **2013**, *200*, 367-371; g) A. Becker, B. K. Thakur, J. M. Weiss, H. S. Kim, H. Peinado, D. Lyden, *Cancer Cell* **2016**, *30*, 836-848.

[2] a) M. P. Bebelman, P. Bun, S. Huveneers, G. van Niel, D. M. Pegtel, F. J. Verweij, *Nat. Protoc.* **2020**, *15*, 102-121; b) C. Théry, M. Ostrowski, E. Segura, *Cell. Mol. Immunol.* **2009**, *9*, 581-593; c) T. Tian, Y. Wang, H. Wang, Z. Zhu, Z. Xiao, *J. Cell. Biochem.* **2010**, 111, 488-496; d) A. E. Morelli, A. T. Larregina, W. J. Shufesky, M. L. G. Sullivan, D. B. Stolz, G. D. Papworth, A. F. Zahorchak, A. J. Logar, Z. Wang, S. C. Watkins, L. D. Falo, Jr, A. W. Thomson, *Blood* **2004**, *104*, 3257-3266.

[3] a) E. van der Pol, A. N. Böing, P. Harrison, A. Sturk, R. Nieuwland, *Pharmacol. Rev.* **2012**, 64, 676-705; b) C. Subra, D. Grand, K. Laulagnier, A. Stella, G. Lambeau, M. Paillasse, P. De Medina, B. Monsarrat, B. Perret, S. Silvente-Poirot, M. Poirot, M. Record, *J. Lipid. Res.* **2010**, *51*, 2105-2120.

[4] a) J. C. Shillcock, R. Lipowsky, *Nat. Mater.* **2005**, *4*, 225-228; b) A. Rørvig-Lund, A. Bahadori, S. Semsey, P. M. Bendix, L. B. Oddershede, *Nano Lett.* **2015**, *15*, 4183-4188; c) B. Gong, B.-K. Choi, J.-Y. Kim, D. Shetty, Y. H. Ko, N. Selvapalam, N. K. Lee, K. Kim, *J. Am. Chem. Soc.* **2015**, *137*, 8908-8911; d) S. Varlas, R. Keogh, Y. Xie, S. L. Horswell, J. C. Foster, R. K. O'Reilly, *J. Am. Chem. Soc.* **2019**, *141*, 20234-20248; e) N.-N. Deng, M. Yelleswarapu, L. Zheng, W. T. S. Huck, *J. Am. Chem. Soc.* 2017, 139, 587-590; f) Y. Zhou, D. Yan, *Angew. Chem., Int. Ed.* **2005**, *44*, 3223-3226; g) J. Steinkühler, R. L. Knorr, Z. Zhao, T. Bhatia, S. M. Bartelt, S. Wegner, R. Dimova, R. Lipowsky, *Nat. Commun.* **2020**, *11*, 905; h) T. Litschel, B. Ramm, R. Maas, M. Heymann, P. Schwille, *Angew. Chem., Int. Ed.* **2018**, *57*, 16286-16290; i) Y. Zhou, D. Yan, *J. Am. Chem. Soc.* **2005**, *127*, 10468-10469.

[5] I. M. Henderson, W. F. Paxton, *Angew. Chem., Int. Ed.* **2014**, *53*, 3372-3376.

[6] W. Zong, S. Ma, X. Zhang, X. Wang, Q. Li, X. Han, *J. Am. Chem. Soc.*

2017, *139*, 9955-9960.

[7] a) J. Mei, N. L. C. Leung, R. T. K. Kwok, J. W. Y. Lam, B. Z. Tang, *Chem. Rev.* **2015**, *115*, 11718-11940; b) J. Li, J. Wang, H. Li, N. Song, D. Wang, B. Z. Tang, *Chem. Soc. Rev.* **2020**, *49*, 1144-1172; c) H.-Q. Peng, B. Liu, P. Wei, P. Zhang, H. Zhang, J. Zhang, K. Li, Y. Li, Y. Cheng, J. W. Y. Lam, W. Zhang, C.-S. Lee, B. Z. Tang, *ACS Nano* **2019**, *13*, 839-846; d) J. Li, K. Liu, H. Chen, R. Li, M. Drechsler, F. Bai, J. Huang, B. Z. Tang, Y. Yan, *ACS Appl. Mater. Interfaces* **2017**, *9*, 21706-21714.

[8] a) J. Li, K. Shi, M. Drechsler, B. Z. Tang, J. Huang, Y. Yan, *Chem. Commun.* **2016**, *52*, 12466-12469; b) J. Li, K. Liu, Y. Han, B. Z. Tang, J. Huang, Y. Yan, *ACS Appl. Mater. Interfaces* **2016**, *8*, 27987-27995.

[9] a) Y. Yan, A. de Keizer, M. A. Cohen Stuart, N. A. M. Besseling, *Soft Matter* **2009**, *5*, 790-796; b) L. Xu, L. Jiang, M. Drechsler, Y. Sun, Z. Liu, J. Huang, B. Z. Tang, Z. Li, M. A. Cohen Stuart, Y. Yan, *J. Am. Chem. Soc.* **2014**, *136*, 1942-1947; c) Y. Lan, L. Xu, Y. Yan, J. Huang, A. de Keizer, N. A. M. Besseling, M. A. Cohen Stuart, *Soft Matter* **2011**, *7*, 3565-3570.

[10] Y. Yan, Y. Lan, A. Keizer, M. Drechsler, H. V. As, M. C. Stuart, N. A. M. Besseling. *Soft Matter*, **2010**, *6*, 3244-3248.

[11] a) K. Li, Y. Lin, C. Lu, *Chem. - Asian J.* **2019**, *14*, 715-729; b) W. Guan, W. Zhou, C. Lu, B. Z. Tang, *Angew. Chem., Int. Ed.* **2015**, *54*, 15160-15164; c) Z. Wang, J. Nie, W. Qin, Q. Hu, B. Z. Tang, *Nat. Commun.* **2016**, *7*, 12033; d) J. Liang, B. Z. Tang, B. Liu, *Chem. Soc. Rev.* **2015**, 44, 2798-2811; e) Z. Wang, X. He, T. Yong, Y. Miao, C. Zhang, B. Zhong Tang, *J. Am. Chem. Soc.* **2020**, *142*, 512-519; g) S. Xu, Y. Duan, B. Liu, *Adv. Mater.* **2020**, *32*, 1903530.

[12] a) F. Ding, Q. Mou, Y. Ma, G. Pan, Y. Guo, G. Tong, C. H. J. Choi, X. Zhu, C. Zhang, *Angew. Chem., Int. Ed.* **2018**, *57*, 3064-3068; b) Q. Sun, Z.

Kang, L. Xue, Y. Shang, Z. Su, H. Sun, Q. Ping, R. Mo, C. Zhang, *J. Am. Chem. Soc.* **2015**, *137*, 6000-6010; c) M. Zheng, T. Jiang, W. Yang, Y. Zou, H. Wu, X. Liu, F. Zhu, R. Qian, D. Ling, K. McDonald, J. Shi, B. Shi, *Angew. Chem., Int. Ed.* **2019**, *58*, 4938-4942; d) O. S. Fenton, K. J. Kauffman, R. L. McClellan, J. C. Kaczmarek, M. D. Zeng, J. L. Andresen, L. H. Rhym, M. W. Heartlein, F. DeRosa, D. G. Anderson, *Angew. Chem., Int. Ed.* **2018**, *57*, 13582-13586.

[13] a) B. Kumar, S. Koul, L. Khandrika, R. B. Meacham, H. K. Koul, *Cancer Res.* **2008**, *68*, 1777-1785; b) T. P. Szatrowski, C. F. Nathan, *Cancer Res.* **1991**, *51*, 794-798.